DOI:10.1190/segam2019-3214754.1

Innovative Automatic Fault Detection using a Volume 3D Scanning Method

Sven Philit, Eliis
Sébastien Lacaze, Eliis*
Fabien Pauget, Eliis

Summary

We present in this work an innovative method for the automatic detection and creation of faults in 3D seismic data as an alternative to the manual and cumbersome fault interpretation. Our method consists in a workflow divided in three steps: 1) the creation of an attribute, the Fault Plane detecting the localization of the deformation, 2) the creation of an attribute corresponding to the skeleton of the deformation, and 3) the faults extraction. We applied this automatic workflow to the well-known F03 block, offshore Netherlands, to show that accurate results are obtained. On top of saving a drastic amount of time to the interpretation, our approach is innovative in the sense that the workflow remains simple, customizable, hence adaptable to various structural settings, and is independent of large data set to yield reliable fault sets.

Introduction

For many years, seismic interpreters have struggled to pick faults manually on the seismic to produce a structural constraint to characterize the sealing settings of the reservoirs. This manual interpretation being very laborious, many authors have tried to create attributes, often derived from the coherency (e.g. Bahorich et al. 1995; Gibson et al., 2003) or the semblance (Hale, 2013; Wu and Fomel, 2018), to identify the fault locations. More recently, attempts have been realized to detect the faults via the machine learning approach (Guitton et al., 2017; Wu et al. 2018, Guo et al., 2018; Ma et al., 2018; Zhao and Mukhopadhyay, 2018). Yet, the results of this approach remain for now questionable in 3D. Indeed, one of the main flaws with this method is that a dramatic amount of seismic data requires being shared and tested to increase the reliability of the results.

In this work, we introduce a new method for the automatic fault detection. We show through a case study that our automatized workflow yields consistent and accurate results, and offers the advantage of being customizable and independent of large seismic database.

Methodology

We present here the methodology used in our work to go from the creation of an attribute highlighting the localized deformation likely to correspond to faults, to the extraction of fault objects that could subsequently be refined by the interpreter.

The first step of the workflow consists in creating from the seismic (Fig. 1a) an attribute where localized deformation is highlighted. To do so, we compute the *Fault Plane*. This attribute is derived from a structural attribute (in this study an optimized variance – Fig. 1b) from which, at each voxel position, a scanning ellipse of a specific length and height (both pondered by a Gaussian function) is used to sum the attribute in all directions and retain the maximum sum from all combinations (Fig. 1b zooms). The Fault Plane attribute (Fig. 1c) is made of these maximum sums (normalized between 0 and 1), whose values are assigned to their respective voxel. The length and height of the scanning ellipse as well as the dip range, the dip and azimuth increments of the scanning can be controlled to optimize the fault detection as a function of the expected dimension and density of the deformation in the seismic cube. In this work, we chose for the scanning a range of azimuths from 0° to 360° with a 15° increment, and a range of dips from 70° to 90° with an increment angle of 5°.

In a second step, we remove the background deformation of the Fault Plane volume to only preserve the skeleton of the deformation, potentially corresponding to the faults. This is the *Thinned Fault Plane* attribute (Fig. 1d). To do so, the extrema values of the Fault Plane attribute are computed; they correspond to the greatest gradient vector on each time slice of the Fault Plane volume.

The third step aims at extracting and creating fault objects and involves several sub-steps. First, from the Thinned Fault Plane volume, groups of about 50 neighboring voxels are used to create *unit patches* (Fig. 1e). To get free from noise effects, these unit patches are ignored if their planarity falls below a determined threshold. Secondly, these unit patches are merged to form *elementary fault segment* (Fig. 1f). To guaranty an accurate geometry relative to the deformation skeleton, this merge is achieved by minimizing a cost function corresponding to the integral of the distance between the elementary fault segment solutions and the Thinned Fault Planes' skeleton. Finally, elementary fault segments whose dimension is above a controllable threshold are transformed into fault sticks objects. Sticks are created along the line direction (Inline or Xline) closest to the perpendicular of the azimuth of the elementary fault segment. The sampling of the fault sticks along the lines can be adapted to control the resolution of the final fault objects. In this study, faults sticks are created every 5 lines. The different groups of fault sticks are then interpolated into surfaces (Fig. 1f in 3D).

10.1190/segam2019-3214754.1

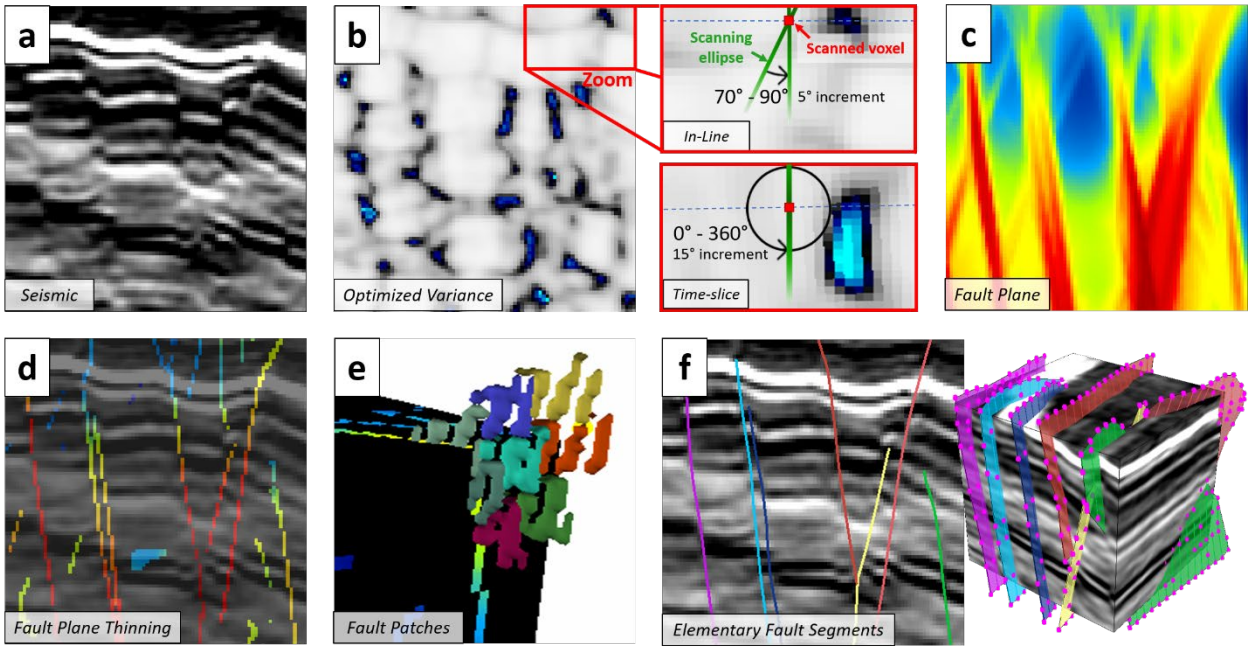

Figure 1. (a) Seismic data used as input for the automatic fault detection workflow. (b) Optimized Variance. The zoom-frames show schematically how the scanning ellipse works out the maximum sums at each voxel location. (c) Fault Plane attribute. (d) Thinned Fault Plane attribute overlain on the seismic. (e) Group of fault patches. (f) Elementary fault segments in 2D and 3D; the 3D view displays the fault stick increment.

The ultimate stage of the processing would consist in filtering and sorting the raw output of the elementary fault segments to eliminate artifact fault planes potentially linked to boundary effects from the Thinned Fault Plane data, and eventually in merging the elementary fault segments to get sets of geologically consistent (in terms of geometry) faults.

Case Study

We tested the automatic workflow presented before on the F03 seismic block, of 500 km^2 area and about 3.5 s in vertical extension (corresponding to 2.8 GB of data), offshore Netherlands (Fig. 2a), in the Central Graben where gas presence has long been suspected (e.g. Schroot and Schüttenhelm, 2003). The block encompasses a series of deposits (Fig. 2b) ranging from Triassic marine-evaporitic sediments, to Early to early Late Jurassic marine shales to carbonates and minor clastic sediments, and then Late Jurassic and Early Cretaceous continental clastic sediments (Van Wijhe, 1987). Late Cretaceous is mainly made of chalk. Paleogene and Neogene are characterized by marine clastic sediments, with the deposition of prograding lowstand clinoforms during Miocene (Sørensen et al., 1997). The whole series is locally marked by several families of normal faults striking NNE-SSW and WNW-ESE developed during a rifting that lasted from Triassic to Middle Jurassic - Early Cretaceous (Verreussel et al., 2018), interrupted by a phase of thermal uplift and volcanic activity during middle Jurassic (Partington et al., 1993). In addition, the whole Jurassic and Cretaceous deposits are locally deformed by salt tectonics, with an uplifted salt dome originating from the Triassic. In this study, although we applied the workflow to the whole seismic cube, we particularly focused on the Jurassic and Cretaceous intervals where the deformation contrast is striking, and willingly decided to ignore the Paleogene siliciclastic interval impacted by overpressure-linked polygonal faults (Verweij et al., 2012) to avoid confusion when presenting the results.

With a hardware setting of 16 GB of RAM and a 2.2 GB processor, the result of the automatized workflow is available after about 3 hours of computation. The result shows that the density of deformation is well captured by the Fault Plane attribute (Fig. 3a and 3b); the skeleton of the Thinned Fault Plane follows the same trend. The result of the extraction step yields a total of 3378 elementary fault segments where the fault network in the Jurassic series is clearly captured and the contrast with the little deformed Early Cretaceous chalk interval is neat (Fig. 3b).

Most of the elementary fault segments correspond to actual faults, and covers most of the faults of the investigated area. The few faults that are not intercepted correspond to small

DOI:10.1190/segam2019-3214754.1

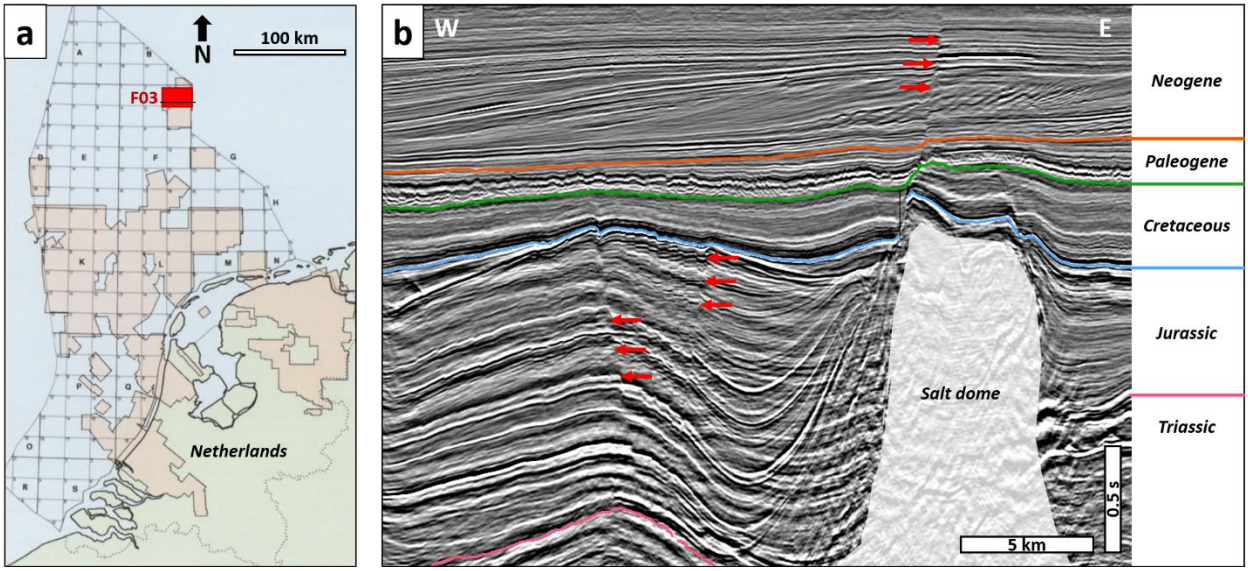

Figure 2. (a) Location of the F03 seismic bloc used in this study, offshore Netherlands (modified after Rondeel et al., 1996). (b) Representative seismic InLine from the F03 seismic block, showing the typical geological settings of the area studied for the application of the automatic fault extraction workflow. Faults linked to the Mesozoic rifting and local salt tectonic are pointed by the red arrows.

faults (in terms of dimension) or noisy areas. Whereas small faults could be captured by decreasing the threshold parameters of the fault extraction step, the noisy areas would remain blind as the Fault Plane attribute could not detect any clear lateral variation in the input signal. For the same reason, theoretically, even if the structural context of the chosen area does not allow controlling this, a pure strike-slip displacement (without vertical component) could not be captured by the proposed method. In F03, we also note that a minority of extracted elementary fault segments corresponds to planes following steep reflectors, hence representing a potential bias in the method.

After filtering, sorting and merging (difference shown between top and bottom of Fig. 3c), the number of geologically consistent faults falls to 1307, among which several sets can easily be distinguished with strike, dip, and dimension filtering tools. In the case of this study, we highlighted three distinct fault sets, respectively striking N-S, WSW-ENE and WNW-ESE corresponding to the different phases of Jurassic to Early Cretaceous rifting (Fig. 3d). Major faults linked to the Cretaceous to Tertiary salt tectonic are also perfectly captured.

We note that the method could allow extracting faults from the Paleogene polygonal fault interval, but we would have to

- Reduce the length and height of the scanning ellipse,
- Apply a lower dimension threshold during the fault extraction step.

As a result, many small faults, not necessary to a proper structural interpretation, would have polluted the rest of the seismic volume.

Conclusions

To reduce the interpretation time of a seismic volume and the traditional and cumbersome fault picking, we developed an automatic method for fault interpretation optimization. This method relies on three main steps, the Fault Plane attribute creation, the Thinned Fault Plane attribute creation, and the fault extraction to detect and eventually create elementary fault segments at the location of the faults. This workflow benefits from being simple and customizable in the sense that the interpreter can choose the input volumes and parameters adapted to the structural style of the investigated seismic at each step of the workflow. Additionally, contrary to the machine learning approach, this method is independent from the sharing of a large database to properly train the algorithms. Potential improvements lie in automating the filtering and merging of the elementary fault segments as a function of their vicinity, strike and dip correspondence to optimize the creation geologically-consistent faults after the detection. The accuracy of the obtained results allows considering industrial implementation soon.

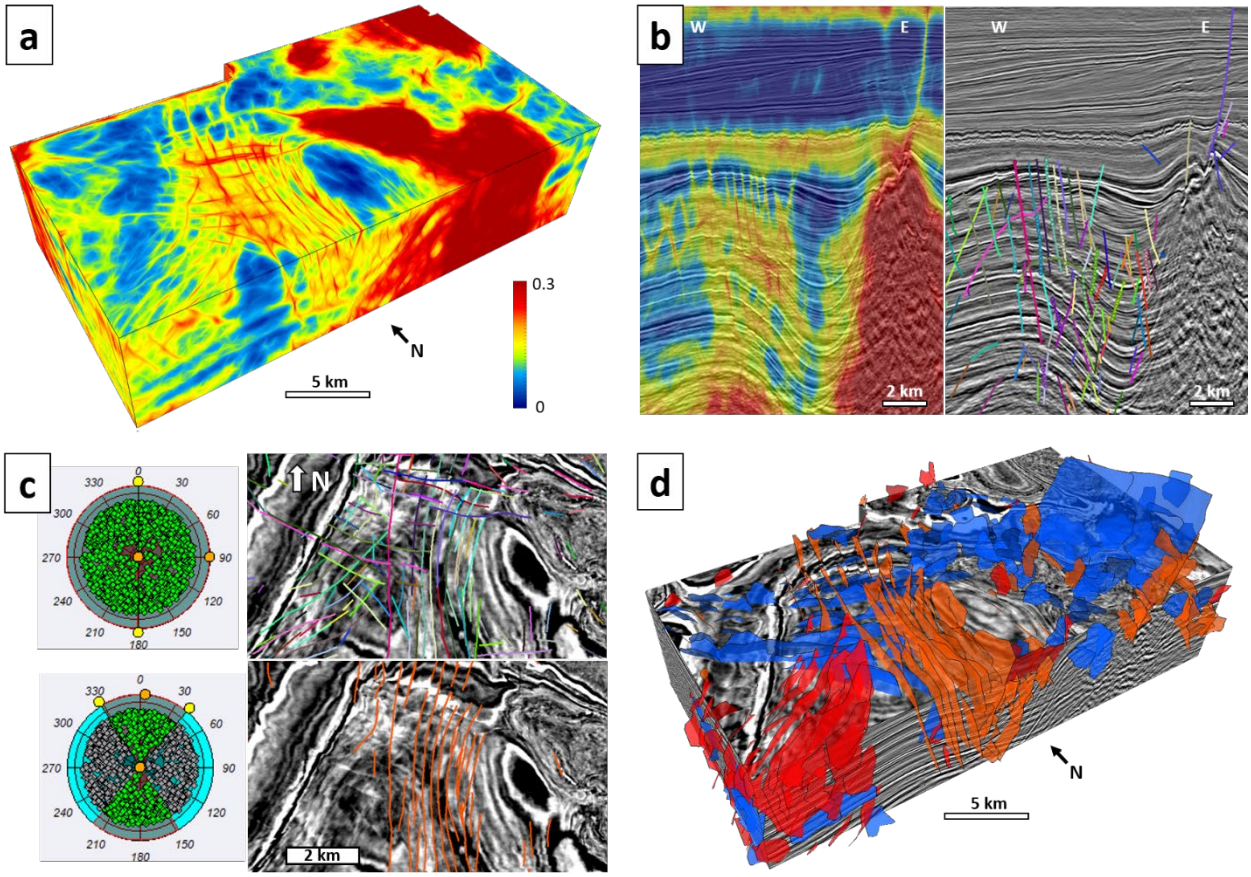

Figure 3. (a) Cropped 3D F03 bloc showing the Fault Plane attribute from near-to Jurassic to near-bottom Jurassic. (b) Left: Blending of the Fault Plane on the seimsic in InLine; Right: same seismic InLine with the outputed raw elementary fault segments (elementary fault segments from the Paleogene interval were ignored). (c) Top: Outputed elementary fault segments in time-slice; Bottom: the faults after orientation filtering and merging. (d) Same cropped volume as in (a) showing the seimic and the 3 distinct fault sets extracted from the automatic fault extraction workflow, and after semi-automatic orientation filtering and merging.

Acknowledgements

The authors would like to thank the TNO and Dutch government for providing access to the F03 seismic data utilized in this study.

REFERENCES

Bahorich, M., and S. Farmer, 1995, 3-D seismic discontinuity for faults and stratigraphic features: The coherence cube: 65th Annual International Meeting, SEG, Expanded Abstracts, 93–96, doi: https://doi.org/10.1190/1.1887523.

Gibson, D., M. Spann, and J. Turner, 2003, Automatic fault detection for 3D seismic data: Proceedings of the 7th Digital Image Computing: Techniques and Applications, 821–830.

Guitton, A., H. Wang, and W. Trainor-Guitton, 2017, Statistical imaging of faults in 3D seismic volumes using a machine learning approach: 87th Annual International Meeting, SEG, Expanded Abstracts, 2045–2049, doi: https://doi.org/10.1190/segam2017-17589633.1.

Guo, B., L. Li, and Y. Luo, 2018, A new method for automatic seismic fault detection using convolutional neural network: 88th Annual International Meeting, SEG, Expanded Abstracts, 1951–1955, doi: https://doi.org/10.1190/segam2018-2995894.1.

Hale, D., 2013, Methods to compute fault images, extract fault surfaces, and estimate fault throws from 3D seismic images: Geophysics, **78**, no. 2, O33–O43, doi: https://doi.org/10.1190/geo2012-0331.1.

Ma, Y., X. Ji, N. BenHassan, and Y. Luo, 2018, A deep-learning method for automatic fault detection: 88th Annual International Meeting, SEG, Expanded Abstracts, 1941–1945, doi: https://doi.org/10.1190/segam2018-2984932.1.

Partington, M. A., B. C. Mitchener, N. J. Milton, and A. J. Fraser, 1993, Genetic sequence stratigraphy for the North Sea Late Jurassic and Early Cretaceous: Distribution and prediction of Kimmeridgian–Late Ryazanian reservoirs in the North Sea and adjacent areas: Geological Society, London, Petroleum Geology Conference Series 4, 347–370, doi: https://doi.org/10.1144/0040347.

Rondeel, H. E., D. A. J. Batjes, and W. H. Nieuwenhuijs, 1996, Geology of gas and oil under the Netherlands: The Royal and Mining Society of the Netherlands-KNGMG.

Schroot, B. M., and R. T. E. Schüttenhelm, 2003, Expressions of shallow gas in the Netherlands North Sea: Netherlands Journal of Geosciences, **82**, 91–105, doi: https://doi.org/10.1017/S0016774600022812.

Sørensen, J. C., U. Gregersen, M. Breiner, and O. Michelsen, 1997, High-frequency sequence stratigraphy of Upper Cenozoic deposits in the central and southeastern North Sea areas: Marine and Petroleum Geology, **14**, 99–123, doi: https://doi.org/10.1016/S0264-8172(96)00052-9.

Van Wijhe, D. H., 1987, Structural evolution of inverted basins in the Dutch offshore. Tectonophysics, **137**, 171–219, doi: https://doi.org/10.1016/0040-1951(87)90320-9.

Verreussel, R. M. C. H., R. Bouroullec, D. K. Munsterman, K. Dybkjær, C. R. Geel, A. J. P. Houben, P. N. Johannessen, and S. J. Kerstholt-Boegehold, 2018, Stepwise basin evolution of the Middle Jurassic–Early Cretaceous rift phase in the Central Graben area of Denmark, Germany and The Netherlands: Geological Society, London, Special Publications 469, 305–340, doi: https://doi.org/10.1144/SP469.23.

Verweij, J. M., H. J. Simmelink, J. Underschultz, and N. Witmans, 2012, Pressure and fluid dynamic characterisation of the Dutch subsurface: Netherlands Journal of Geosciences, **91**, 465–490, doi: https://doi.org/10.1017/S0016774600000342.

Wu, X., and S. Fomel, 2018, Automatic fault interpretation using optimal surface voting: 88th Annual International Meeting, SEG, Expanded Abstracts, 1639–1643, doi: https://doi.org/10.1190/segam2018-2997460.1.

Wu, X., Y. Shi, S. Fomel, and L. Liang, 2018, Convolutional neural networks for fault interpretation in seismic images, 88th Annual International Meeting, SEG, Expanded Abstracts, 1946–1950, doi: https://doi.org/10.1190/segam2018-2995341.1.

Zhao, T., and P. Mukhopadhyay, 2018, A fault-detection workflow using deep learning and image processing, 88th Annual International Meeting, SEG, Expanded Abstracts, 1966–1970, doi: https://doi.org/10.1190/segam2018-2997005.1.